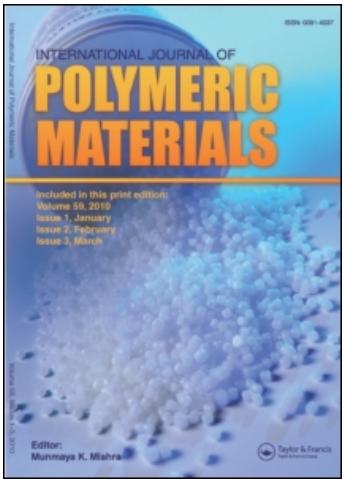

International Journal of Polymeric Materials
Publication details, including instructions for authors and subscription information:
http://www.informaworld.com/smpp/title~content=t713647664

Effects of Fiber Morphology in Short Fiber Reinforced Composites

H. G. Kim[a]; D. J. Lee[b]
[a] Dept. of Mechanical Engineering, Jeonju University, Jeonju, Korea [b] Dept. of Mechanical Engineering, Yeungnam University, Gyongsan, Korea

To cite this Article Kim, H. G. and Lee, D. J.(1995) 'Effects of Fiber Morphology in Short Fiber Reinforced Composites', International Journal of Polymeric Materials, 28: 1, 61 — 76
To link to this Article: DOI: 10.1080/00914039508012088
URL: http://dx.doi.org/10.1080/00914039508012088

Intern. J. Polymeric Mater., 1995, Vol. 28, pp. 61–76
Reprints available directly from the publisher
Photocopying permitted by license only

Effects of Fiber Morphology in Short Fiber Reinforced Composites

H. G. KIM

Dept. of Mechanical Engineering, Jeonju University, Jeonju, 560-759, Korea

and

D. J. LEE

Dept. of Mechanical Engineering, Yeungnam University, Gyongsan, 712-749, Korea

(Received July 25, 1994)

The upper and lower bounds of fiber/fiber interaction effects induced by the different fiber morphologies in a short fiber reinforced composite were studied using an axisymmetric finite element (FE) model that employs a periodic hexagonal array of elastic short fibers embedded in an elastoplastic matrix. An equivalent representative volume element (RVE) was modeled to maintain vertical and horizontal constrained boundary conditions for the reduction of modeling efforts. The internal stress fields were evaluated for the ideally aligned single fiber model and compared to a staggered model. It was found that both fiber and matrix stresses in a staggered fiber model are significantly altered from those of the perfectly aligned case. Finally, the hydrostatic stresses in the matrix along the fiber/matrix interface and the evolution of matrix plasticity for each model were illustrated.

KEY WORDS Morphological effect, aligned and staggered fiber model, hydrostatic stress, plasticity.

1. INTRODUCTION

For the analysis and design of composites, finite element analysis (FEA) has become a popular tool because of its versatile micromechanical modeling capability. One of the earliest FEA work in this area is due to Iremonger and Wood.[1] They studied stresses in the region of a broken fiber using a 2-D plane stress FEA and found that the stress concentrations become more significant as fibers approach to themselves. They also found that higher stress concentrations exist at the fiber/matrix interface if the matrix end gap is a void compared to a filled matrix. Using an axisymmetrix FE model, Carrara and McGarry[2] pursued to describe the distribution of stresses near the tip of the fiber for the different end geometries and modulus ratios. The photoelastic investigation combined with 2-D FEA was also performed to understand the discontinuity effects between fibers.[3] As a more systematic study, Barker and MacLaughlin[4] identified three primary parameters, such as, end gap size, fiber volume fraction and modulus ratio to study on discontinuity effects.

All the above analyses were limited to a linear elasticity and so did not permit localized yielding behavior in the matrix. For performing elastoplastic FEA, Chen[5] applied *von* Mises-Hencky criterion to each constituent material of a polymer matrix composite (PMC) using 2-D model. The aligned and staggered fiber geometries to define the boundary conditions of a representative volume element (RVE) was first considered by Agarwal *et al.*[6] in a PMC. They studied on the influence of a different fiber geometries to investigate the internal stresses and global composite properties in graphite-epoxy system. However, the boundary conditions they implemented in the staggered fiber model were not verified well in the realistic sense.

On the other hand, Termonia[7] studied to find the stress transfer mechanism for a single fiber model using 2-D finite difference method. He showed that the finite difference approach can provide a useful tool. Subsequently, he investigated the elastic properties of short fiber and particulate filled polymers using his computer model.[8] Recently, Christman *et al.*[9] studied using a 2-D elastic-viscoplastic model and presented that the effect of fiber clustering is substantial for composite strengthening by emphasizing the dependence of ductility on the microstructure of the matrix and on the morphology of the reinforcement. More recently, Papazian and Adler[10] characterized the tensile behavior of the SiC reinforced Al alloy in terms of different heat treatment conditions, and subsequently Levy and Papazian[11] simulated with their experimental results by modeling on transversely aligned and staggered fiber arrangements using 3-D FEA. They concluded that the experimental data is between the aligned and staggered model.

Ideally, evaluating fiber interactions require 3-D multiple fiber models but 3-D models need enormous computation and are expensive. Thus, 2-D models are still popular to investigate qualitative results. However, the quantitative results in 2-D models are inaccurate. Thus, an axisymmetric model which quantitatively provides the similar results for a staggered RVE (SRVE) as a full 3-D model has been developed in this study. This new axisymmetric RVE also provides valuable information on the physical aspects of the local stress variations in the matrix and fiber. Further, these results compare to the idealized aligned RVE (ARVE) for the evaluation of fiber arrangement effects. It was found, using the new axisymmetric RVE, that a fundamental difference exists between the ARVE and SRVE.

2. ANALYSIS

The FE formulations in this work are centered on the elastoplastic analysis with small strain plasticity theory[12,13] using an axisymmetric single reinforcement model. To solve nonlinearity, Newton-Raphson method has been implemented in this study. Consistent with small strain theory, we can write as:

$$\{d\varepsilon^{el}\} = \{d\varepsilon\} - \{d\varepsilon^{pl}\} \tag{1}$$

where $\{d\varepsilon\}$, $\{d\varepsilon^{el}\}$, and $\{d\varepsilon^{pl}\}$ are changes in total, elastic, and plastic strain vectors, respectively. Elastoplastic stress-strain matrix can be solved iteratively, in which the elastic strain vector is updated at each iteration, and the element tangent matrix

is also updated. For a static analysis, the FE discretization process yields a set of simultaneous equations:

$$[K]\{u\} = \{F^a\} \tag{2}$$

where $[K]$ is the stiffness matrix, $\{u\}$ is a set of displacements, and $\{F^a\}$ is a set of applied loads. By Newton-Raphson method, the path dependent non-linearity can be accomplished effectively by using a step by step incremental analysis, i.e., the final load $\{F^a\}$ is reached by stepping the load in increments and performing the Newton-Raphson iterations at each step:

$$[K_{m,n}]\{\Delta u_n\} = \{F^a_m\} - \{F^{nr}_{m,n}\} \tag{3}$$

$$\{u_{n+1}\} = \{u_n\} + \{\Delta u\} \tag{4}$$

where $[K_{m,n}]$ is the tangent stiffness matrix for load step m, and iteration n, $\{F^{nr}_{m,n}\}$ is the restoring force for load step m and iteration n, and $\{F^a_m\}$ is the total applied force at load step m. At each iteration of a load step, both $[K_n]$ and $\{F^{nr}_n\}$ are evaluated based on the configuration given by $\{u_n\}$ and the preset criterion for convergence, i.e. plasticity ratio was used as 1% at all integration points in the model. The element tangent matrix $[K_{e,n}]$ and the element Newton-Raphson restoring vector $\{F^{nr}_{e,n}\}$ in the n^{th} iteration are:

$$[K_{e,n}] = \int_V [B]^T[D_{ep,n}][B]\, dV \tag{5}$$

$$\{F^{nr}_{e,n}\} = \int_V [B]^T[D_{ep,n}]\{\varepsilon^{el}_n\}\, dV \tag{6}$$

where $[B]$ is the strain-displacement matrix, $[D_{ep,n}]$ is the elastoplastic stress-strain matrix. The derivation of $[D_{ep}]$ is as follows. The yield criterion determines the stress level at which yielding is initiated. For an elastoplastic material, a yield function F which is a function of stress $\{\sigma\}$ and quantities $\{\alpha\}$ and κ associated with the hardening rule can be defined. Yielding occurs when

$$F(\{\sigma\}, \{\alpha\}, \kappa) = 0 \tag{7}$$

where κ is the plastic work per unit volume and $\{\alpha\}$ is the translation of yield surface. Specifically, the $\{\alpha\}$ is history dependent, i.e.

$$\{\alpha\} = \int C\{d\varepsilon^{pl}\} \tag{8}$$

$$\kappa = \int \{\sigma\}^T\{d\varepsilon^{pl}\} \tag{9}$$

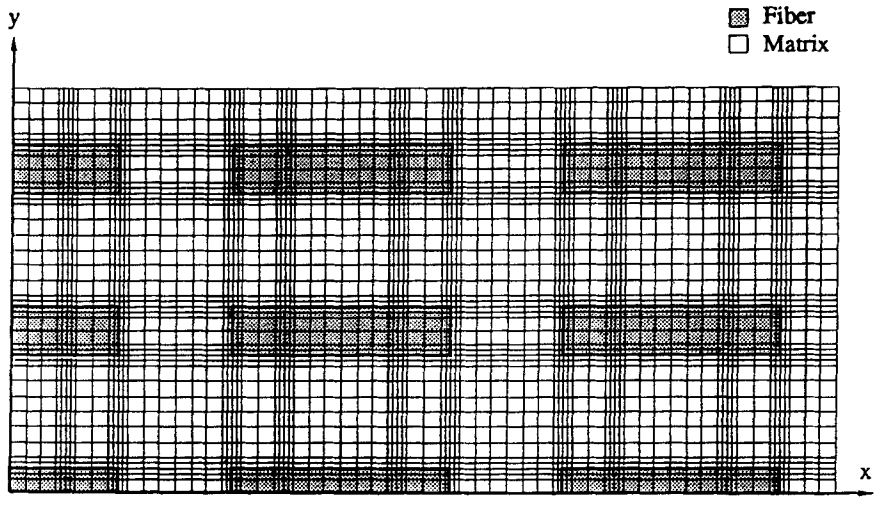

(a)

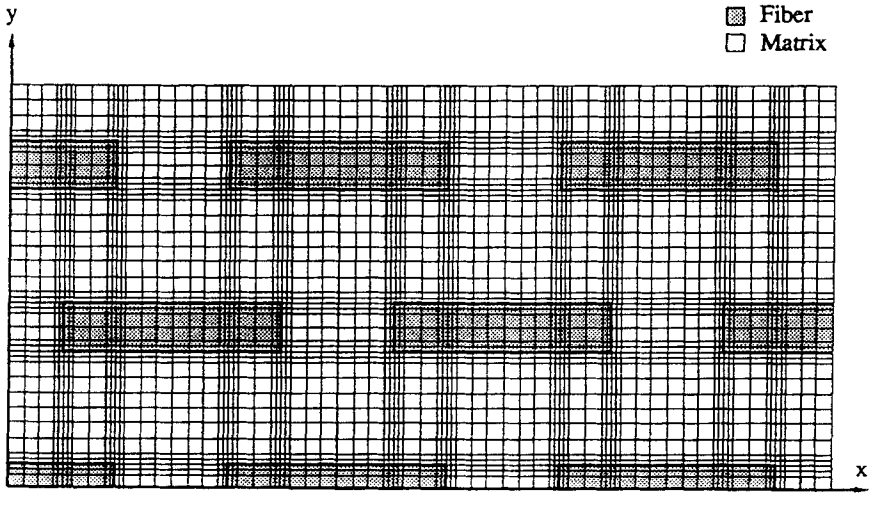

(b)

FIGURE 1 2-D multi-fiber models: (a) Aligned model, (b) Staggered model.

where C is a material parameter. According to *von* Mises theory, yielding begins under any states of stress when the effective stress σ_e exceeds a certain limit, where

$$\sigma_e = \left[\frac{1}{2}\{(\sigma_x - \sigma_y)^2 + (\sigma_y - \sigma_z)^2 + (\sigma_x - \sigma_z)^2\} + 3(\tau_{xy}^2 + \tau_{yz}^2 + \tau_{xz}^2)\right]^{1/2} \quad (10)$$

The flow rule determines the direction of plastic straining. A plastic potential Q

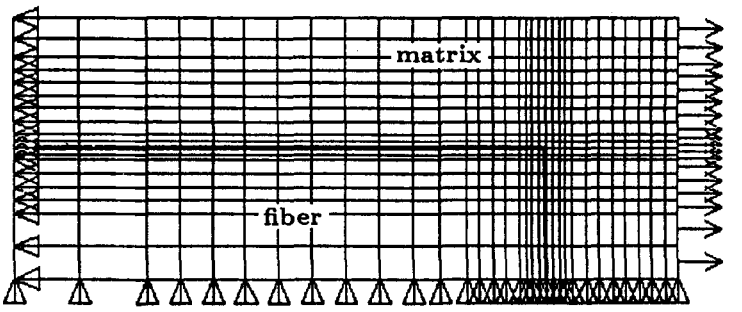

FIGURE 2 FE mesh with the symmetric and loading boundary conditions generated for ARVE.

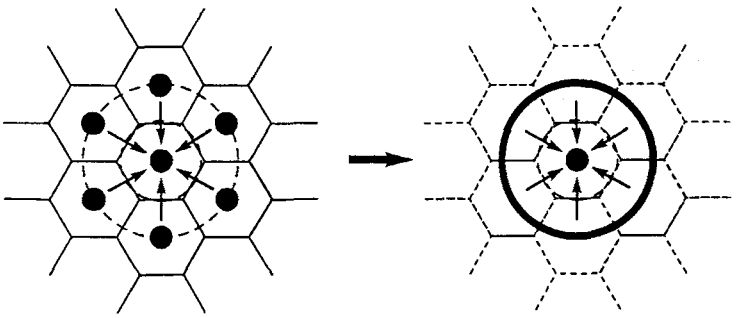

FIGURE 3 A schematic of the procedures from multi-fiber model to axisymmetric model: (a) Hexagonal packing symmetry of fibers, (b) The corresponding equivalent axisymmetric RVE.

which has a unit of stress and is a function of stresses (that determine the direction of plastic straining), $Q = Q(\{\sigma\}, \{\alpha\}, \kappa)$. With λ, a scalar which is called a *plastic multiplier* (that determines the amount of plastic straining), the plastic strain increments are given by

$$\{d\varepsilon^{pl}\} = \lambda \left\{\frac{\partial Q}{\partial \sigma}\right\} \tag{11}$$

where $\{d\varepsilon^{pl}\}$ is the incremental plastic strain. The hardening rule describes the change of the yield surface with progressive hardening, so that the conditions, i.e., the yield surface in stress space. Equation (7) can then be differentiated so that

$$dF = \left\{\frac{\partial F}{\partial \sigma}\right\}^T \{d\sigma\} + \left\{\frac{\partial F}{\partial \alpha}\right\}^T \{d\alpha\} + \frac{\partial F}{\partial \kappa} d\kappa = 0 \tag{12}$$

Noting from equations (8) and (9) that

$$\{d\alpha\} = C\{d\varepsilon^{pl}\} \tag{13}$$

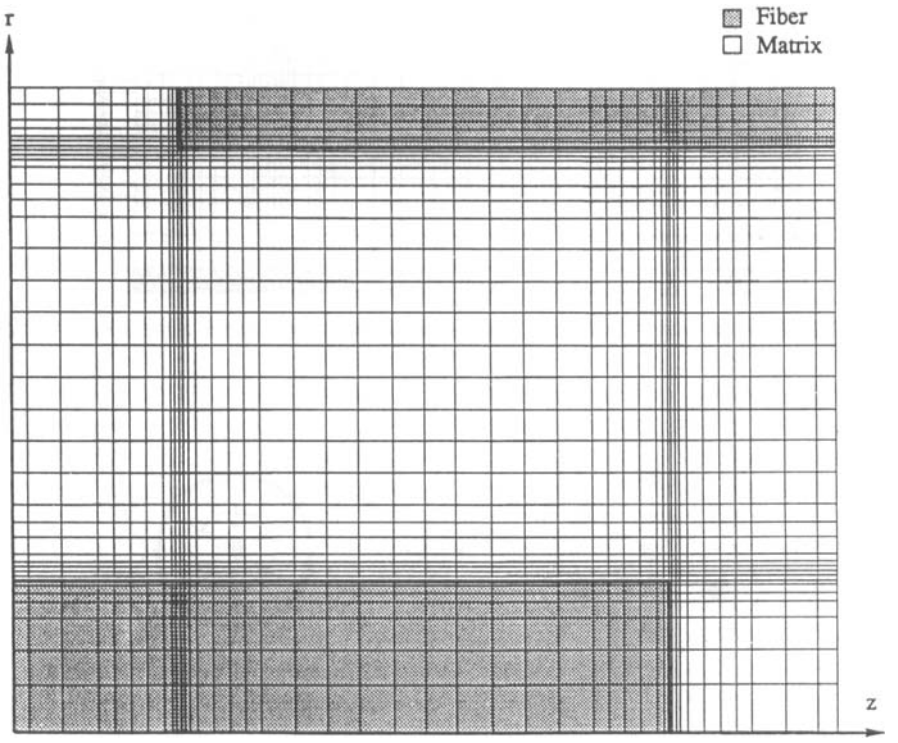

FIGURE 4 FE mesh for the new axisymmetric model with staggered fiber arrangement (SRVE).

$$d\kappa = \{\sigma\}^T\{d\varepsilon^{pl}\} \tag{14}$$

Using equations (13) and (14), equation (12) becomes

$$\left\{\frac{\partial F}{\partial \sigma}\right\}^T \{d\sigma\} + \left\{\frac{\partial F}{\partial \alpha}\right\}^T C\,\{d\varepsilon^{pl}\} + \frac{\partial F}{\partial \kappa}\{\sigma\}^T\{d\varepsilon^{pl}\} = 0 \tag{15}$$

The stress increment can be computed via the elastic stress-strain relations as follows:

$$\{d\sigma\} = [D]\{d\varepsilon^{el}\} = [D](\{d\varepsilon\} - \{d\varepsilon^{pl}\}) \tag{16}$$

Substituting equation (12) into equations (15) and (16) and combining equations (15) and (16):

$$\lambda = \{C_\lambda\}^T\{d\varepsilon\} \tag{17}$$

where

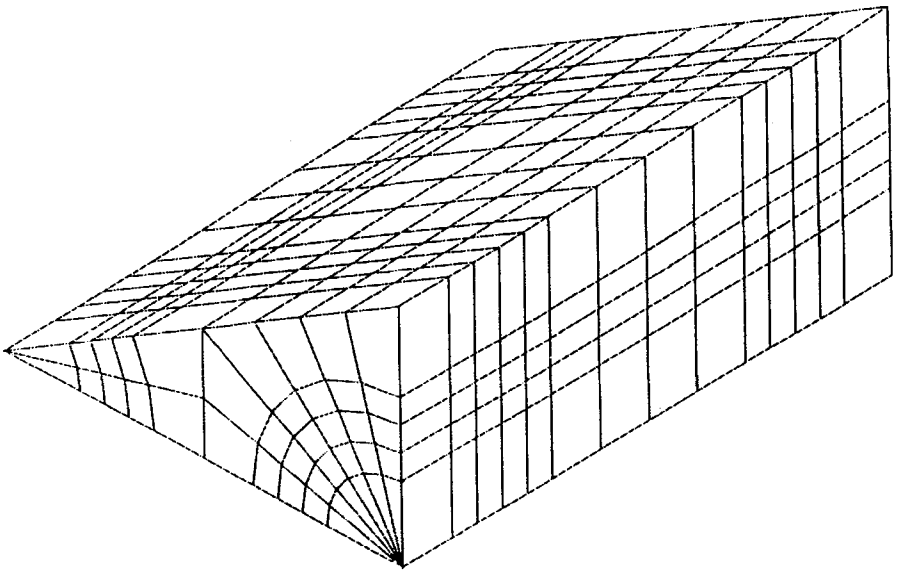

FIGURE 5 3-D FE mesh of the staggered fiber model for rigorous 3-D calculation.

$$\{C_\lambda\} = \frac{\left\{\frac{\partial F}{\partial \sigma}\right\}^T [D]}{\left\{\frac{\partial F}{\partial \sigma}\right\}^T [D]\{d\sigma\} - C\left\{\frac{\partial F}{\partial \alpha}\right\}^T \left\{\frac{\partial Q}{\partial \sigma}\right\} - \frac{\partial F}{\partial \kappa}\{\sigma\}^T \left\{\frac{\partial Q}{\partial \sigma}\right\}} \tag{18}$$

The size of plastic strain increment is therefore related to the total increment in strain, the current stress state and the specific forms of the yield and potential surfaces. The plastic strain increment is then computed using equation (11). The tangent or elastoplastic stress-strain matrix can then be derived by equation (16):

$$\{d\sigma\} = [D](\{d\varepsilon\} - \{d\varepsilon^{pl}\}) \tag{19}$$

Using the definition of $\{d\varepsilon^{pl}\}$ and λ in equations (11) and (17):

$$\{d\sigma\} = [D_{ep}]\{d\varepsilon\} \tag{20}$$

where the elastoplastic matrix $[D_{ep}]$ is

$$[D_{ep}] = [D]\left(1 - \left\{\frac{\partial Q}{\partial \sigma}\right\}\{C_\lambda\}^T\right) \tag{21}$$

Incorporating *associated* flow rule (Plandtl-Reuss equation) and isotropic hardening rule, $Q = F$ and $\{\alpha\} = \{0\}$ have been implemented in this study.

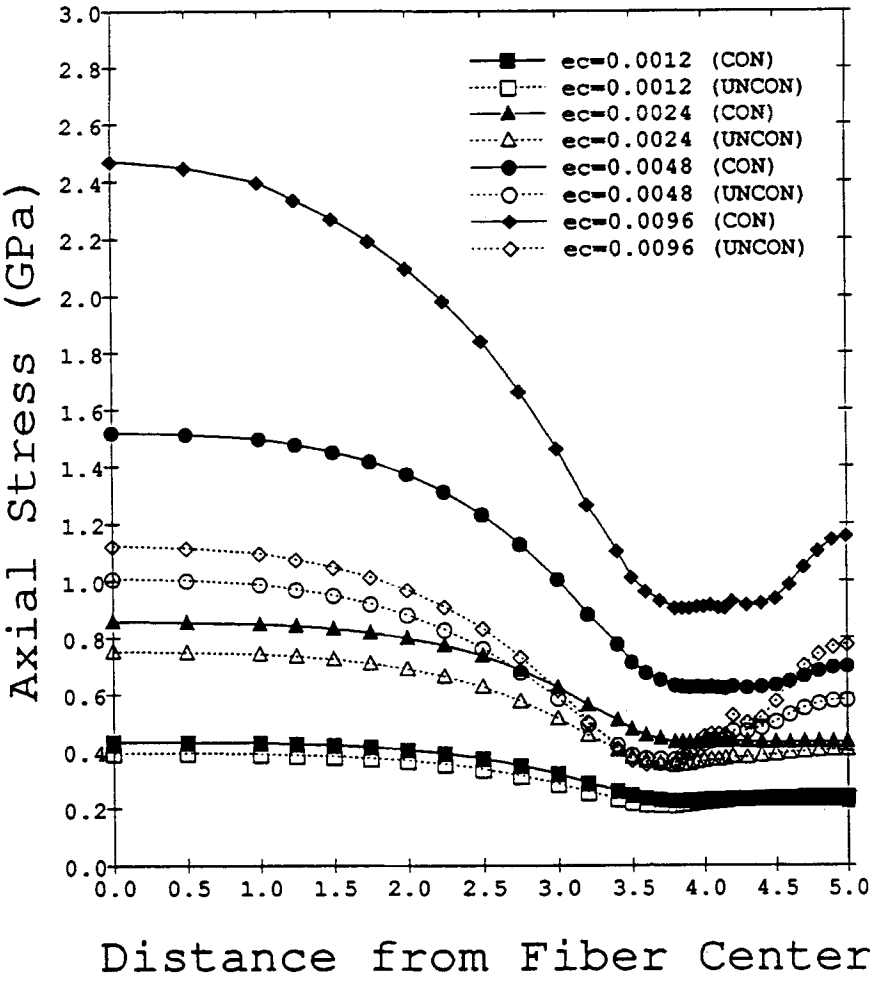

FIGURE 6 Fiber stresses on the center line as a function of normalized distance by whisker radius with and without constraints.

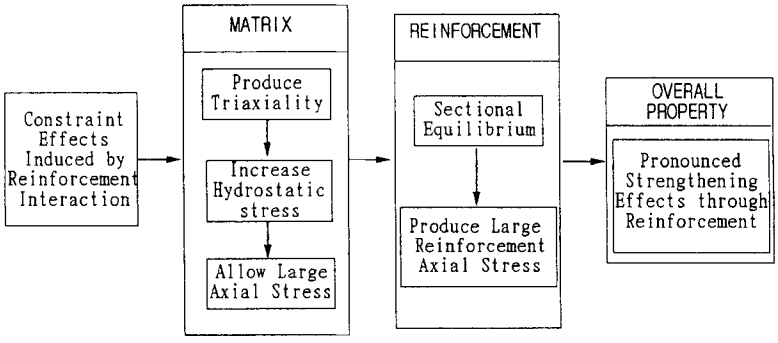

FIGURE 7 Block diagram of composite strengthening mechanism.

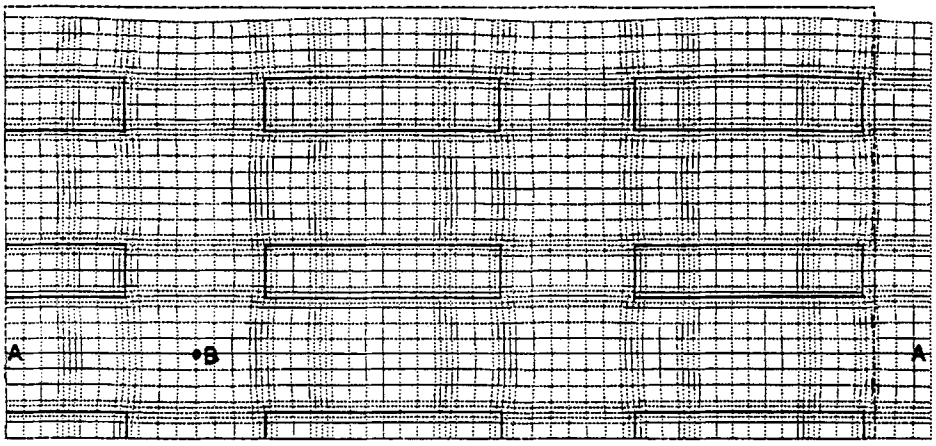

(a)

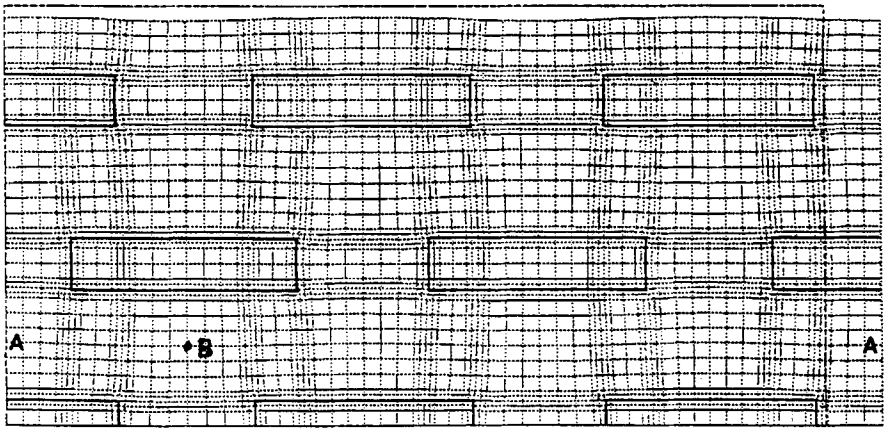

(b)

FIGURE 8 Deformed shape of 2-D multi-fiber models: (a) Aligned model, (b) Staggered model.

3. MODEL

The 2-D multiple fiber model used to develop the physical concepts is shown in Figures 1(a) and (b), respectively for the aligned and staggered fiber geometries. In the very ideal case, where fibers are perfectly aligned, see Figure 1(a), a single fiber axisymmetric model (related to ARVE) would nearly correspond to a 3-D model and fiber interactions can be accounted for by use of cell boundary constraint conditions. It has been reported that this type of morphology (ARVE) gives a upper bound of constraint effect.[9] The FE mesh with symmetric and loading boundary conditions generated for ARVE is shown in Figure 2. However, it is also important to evaluate the morphology having a lower bound of constraint effect as shown in Figure 1(b), called staggered fiber arrangement (related to SRVE).

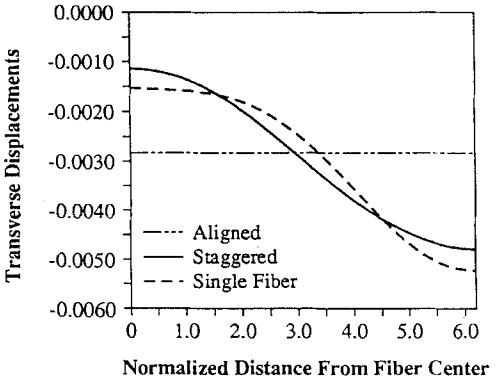

FIGURE 9 Normalized transverse displacement in a 2-D multi-fiber model as a function of distance from fiber center on the RVE boundary.

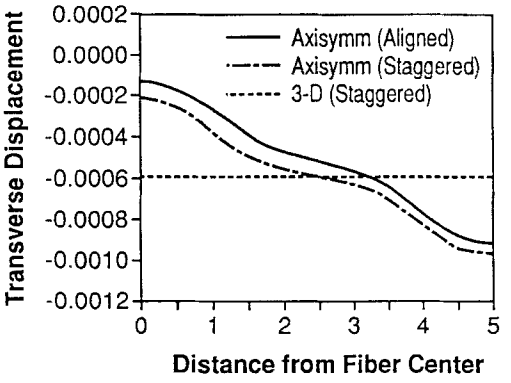

FIGURE 10 Comparison of the transverse displacements along a longitudinal line midway between the fibers at low applied load (ε_c = 0.1% for the new axisymmetric model (SRVE) and the full 3-D model).

In this case, a single fiber axisymmetric model is not appropriate, but a 3-D model would be necessary. The physical basis of the interaction modeling for SRVE is shown in Figures 3(a) and (b). Results of the interaction from neighboring cells are equivalent to a concentric hollow cylinder surrounding the reference fiber. Accordingly, the SRVE is shown in Figure 4. The volume of the concentric cylinder is identical to that of the six neighboring fibers assuming hexagonal packing. The 3-D model to compare the results of the SRVE is shown in Figure 5.

For all models, a uniform reinforcement distribution with an end gap value equal to transverse spacing between reinforcements was selected. The reinforcements were assumed as no reinforcement/matrix debonding allowed for. The FE computations were performed using four and eight noded isoparametric elements for axisymmetric and 3-D models, respectively. In the axisymmetric models, the spatial variable for the axial (mechanical loading) direction is z with the coordinate origin at the reinforcement center, whereas the spatial variable for the radial direction is

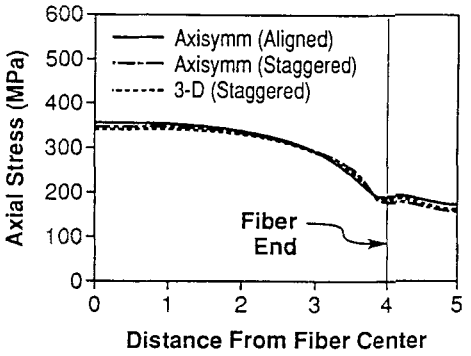

(a)

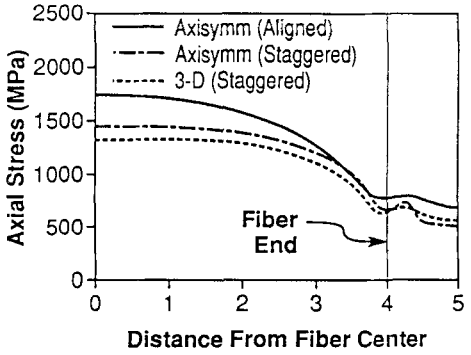

(b)

FIGURE 11 Fiber axial stresses for different models: (a) At low applied load (ε_c = 0.1%), (b) At high applied load (ε_c = 0.6%). The stresses along this interface line in the matrix region between fibers are also included.

r. The constrained boundary condition enforces elastic and plastic constraint by requiring that the radial and axial boundaries of RVE were maintained in the straight manner during deformation.

For fiber input data, linear elastic behavior was employed. From the matrix test data, however, a multi-linear representation of the matrix stress-strain curve was used for elastoplastic matrix behavior. Thus, the stress-strain characteristics of the matrix are defined by the elastic (Young's) modulus, yield stress and multi-linear work hardening rates (tangent moduli). The elastic modulus ratio and Poisson's ratio of fiber to matrix were used as 7.14 and 0.52, respectively. The fiber and matrix materials were assumed to be isotropic and the elastic constants were assumed to be temperature independent, i.e., thermally induced residual stresses were neglected. To obtain tensile stress-strain behavior numerically, the applied far field tensile strain ε_c was loaded from 0 to 1% and 25 small load steps of which step has maximum 20 iterations were used incrementally by $\Delta\varepsilon_c$ = 0.04%. The obtained stress-strain behavior as a function of the elastic modulus ratio, Poisson's ratio and aspect ratio will be discussed later.[14]

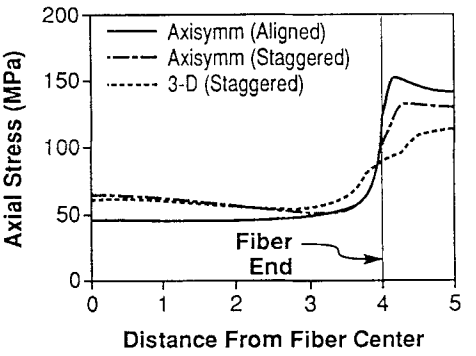

(a)

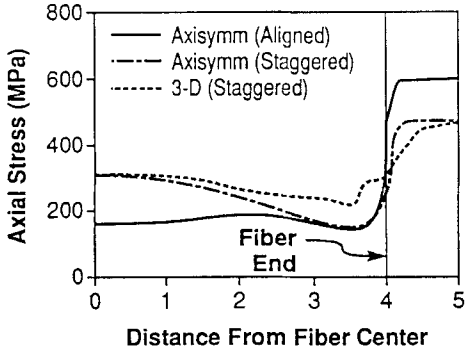

(b)

FIGURE 12 Matrix axial stresses adjacent to the fiber/matrix interface for different models: (a) At low applied load (ε_c = 0.1%), (b) At high applied load (ε_c = 0.6%). The stresses along this interface line in the matrix region between fibers are also included.

4. RESULTS AND DISCUSSION

4.1 Effect of Boundary Conditions

As reported in the previous study,[15] the constraint boundary condition significantly effects on the behavior of deformation and failure mechanisms in discontinuous composites. In this section, constraint effects are assessed using ARVE because it shows the upper bound.[9] Figure 6 shows the fiber stresses of constrained and unconstrained models of ARVE. It is found that the difference of stress values increases significantly as the applied far field strain is increases. The implication of this result indicates that the major composite strengthening mechanism stems from fiber strengthening generated by sectional equilibrium in the axial direction based on tensile triaxiality in the matrix.

It is inferred, by the results of Figure 6, that the composite strengthening mechanism is substantially influenced by fiber/fiber interactions. Figure 7 shows a brief strengthening mechanism in a composite. As discussed in the previous work,[15] the

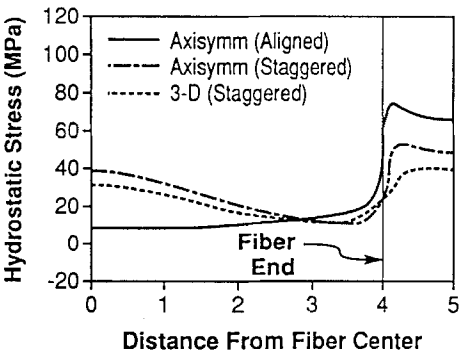

(a)

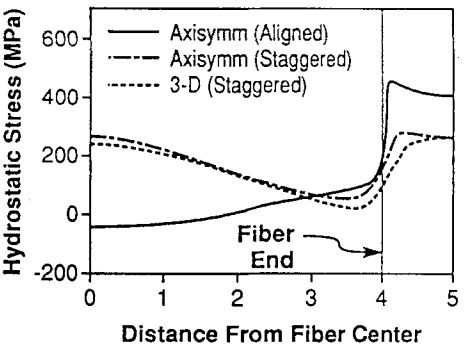

(b)

FIGURE 13 Matrix hydrostatic stresses adjacent to the fiber/matrix interface for different models: (a) At low applied load (ε_c = 0.1%), (b) At high applied load (ε_c = 0.6%). The stresses along this interface line in the matrix region between fibers are also included.

pronounced constraint effects on the hydrostatic stresses stem from the additionally generated tensile triaxiality. This enhancement of hydrostatic stresses results in the expansion of yield surface, which prohibits an extensive plastic deformation. The implication of this mechanism indicates that the major strengthening stems from reinforcement generated by sectional equilibrium in the axial direction based on tensile triaxiality in the matrix.

4.2 Shape of Deformation

The deformed multiple cells for the two cases are shown in Figures 8(a) and (b). It is clear from the figures that for the aligned case any line AA running between the fibers is perfectly straight indicating constraint whereas for the staggered case the same line AA has approximately sinusoidal type of variation which is similar to the kind of displacement profile that is obtained when a single fiber RVE is allowed to deform without constraint. This suggests that the magnitude of matrix constraint be very different for aligned and staggered cases. The quantitative magnitude of the displacement along AA is shown in Figure 9.

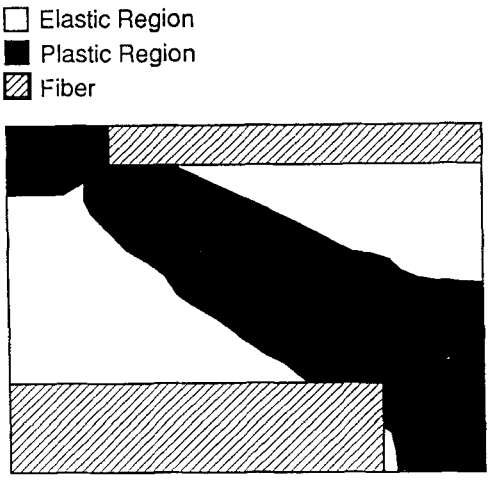

FIGURE 14 The evolution of matrix plasticity for SRVE at $\varepsilon_t = 0.6\%$. Dark region indicates the plastically deformed zone.

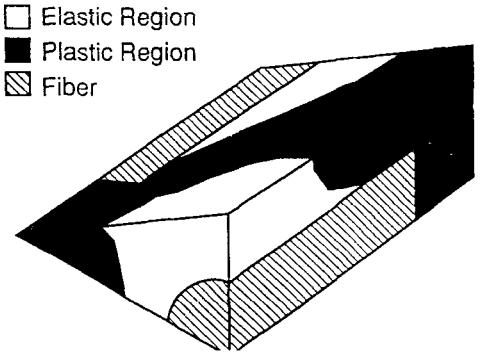

FIGURE 15 The evolution of matrix plasticity for 3-D model at $\varepsilon_t = 0.6\%$. Dark region indicates the plastically deformed zone.

The proper 3-D model results including SRVE results were also considered. The corresponding displacement profile in the 3-D model which is similar to that shown in Figure 9 for the 2-D case is shown in Figure 10. Figure 10 indicates that the results of SRVE give rise to a similar qualitative variation as shown in Figure 9. Further, the magnitude of the displacement obtained by the SRVE compares very well with that obtained by a full 3-D computation. This result establishes the significant difference in constraint effects even for the 3-D case between aligned and staggered models.

4.3 Fiber and Matrix Axial Stresses

In this section, the elastic and elastoplastic results were presented to examine the difference in the behavior between aligned and staggered cases. Here, far field

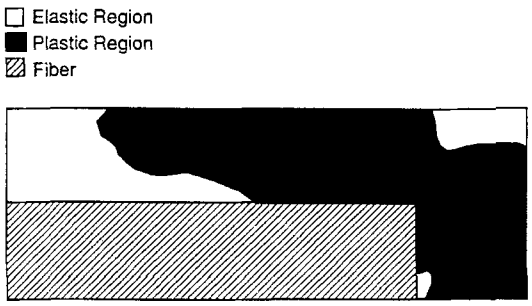

FIGURE 16 The evolution of matrix plasticity for ARVE at $\varepsilon_c = 0.6\%$. Dark region indicates the plastically deformed zone.

elastic strain ε_c was chosen as $\varepsilon_c = 0.1\%$ for the results of elastic analysis and $\varepsilon_c = 0.6\%$ for the results of elastoplastic analysis. The fiber and fiber end gap stresses for the aligned and staggered models (full 3-D and SRVEs) are shown for these two loading cases in Figures 11(a) and (b). It is evident that, in the elastic region, there is a little difference between aligned and staggered fiber geometries. However, in the elastoplastic region, the fiber and fiber end gap stresses are significantly lower in the SRVE case compared to the ARVE case. Concerning to the accuracy of the proposed model, there is a good agreement between the 3-D and SRVE.

Matrix axial stresses, for the two loading cases, adjacent to the fiber/matrix interface line are shown in Figures 12(a) and (b). In the elastic region, there is a little difference in the matrix axial stress between ARVE and SRVE. On the other hand, in the elastoplastic region, the axial matrix stress adjacent of the interface for the ARVE case is about half that for the SRVE case. However, the stresses in the fiber end gap regions are reversed, that is, the matrix axial stress is higher for the ARVE. Again, there is a good agreement between the 3-D and SRVE.

4.4 Matrix Hydrostatic Stresses and Plasticity Evolution

The most dramatic effect of constraint can be seen by viewing the matrix hydrostatic stresses adjacent to the fiber/matrix interface line, see Figures 13(a) and (b). It is shown that the hydrostatic stresses in the matrix adjacent to the fiber/matrix interface is much higher for the SRVE whereas, in the end gap region, those are much higher for the ARVE. It will appear, therefore, that failure mechanisms can be significantly altered by the fiber morphology. In the SRVE, the hydrostatic stresses are about the same both in the enveloping matrix regions as well as in the end gap regions, whereas the high hydrostatic stresses in the ARVE are only obtained in the matrix end gap region. Thus far, matrix failure may be more distributed for the SRVE case whereas much more localized to the matrix end gap region for the ARVE case. Finally, as the difference in plastic zone development for the ARVE and SRVE at $\varepsilon_c = 0.6\%$, the evolution of plasticity for SRVE and 3-D model shows a similar behavior as shown in Figures 14 and 15. However, the plastic zone for ARVE indicates the larger size as can be seen in Figure 16.

5. CONCLUSIONS

A new axisymmetric model (SRVE) was developed to account for fiber/fiber interaction effects, which compare well with a rigorous 3-D RVE. The model was applied to investigate the functional difference between aligned and staggered fiber geometries. It was found that the aligned fiber geometry gives more effective load transfer to fibers with resulting higher fiber stresses. The magnitude and spatial variation of the hydrostatic stresses were significantly different between aligned and staggered geometries suggesting that the fracture micromechanisms can be different for the two cases. It was also quantitatively evaluated, for ARVE and SRVE, that the constraint effects result in a triaxiality in the matrix so that give a difficulty to deform plastically between fibers. Further, the fiber axial stress is fairly sensitive to the constraint effects and thus contributes to the composite strengthening.

References

1. M. J. Iremonger and W. G. Wood, *J. Strain Analysis*, **2**, 239 (1967).
2. A. S. Carrara and F. J. McGarry, *J. Composite Materials*, **2**, 222 (1968).
3. T. F. MacLaughlin, *J. Composite Materials*, **2**, 44 (1968).
4. R. M. Barker and T. F. MacLaughlin, *J. Composite Materials*, **5**, 492 (1971).
5. P. E. Chen, *Polymer Eng. and Sci.*, **11**, 51 (1971).
6. B. D. Agarwal, J. M. Lifsitz and L. J. Broutman, *Fiber Sci. and Tech.*, **7**, 45 (1974).
7. Y. Termonia, *J. Mat. Sci.*, **22**, 504 (1987).
8. Y. Termonia, *J. Mat. Sci.*, **22**, 1733 (1987).
9. T. Christman, A. Needleman and S. Suresh, *Acta Metall.*, **37**, 3029 (1989).
10. J. M. Papazian and P. N. Adler, *Metall Trans.*, A, **21A**, 401 (1990).
11. A. Levy and J. M. Papazian, *Metall Trans.*, A, **21A**, 411 (1990).
12. R. D. Cook, D. S. Malkua and M. E. Plesha, "Concepts and Applications of Finite Element Analysis" (John Wiley & Sons, 1989), 3rd Ed., pp. 163–295.
13. P. C. Kohnke, "ANSYS Theoretical Manual" (Swanson Analysis Systems Inc., Houston, PA, 1989), 5th Ed.
14. D. J. Lee and H. G. Kim, To be published.
15. H. G. Kim and D. J. Lee, *J. the Institute of Industrial Tech*, **22**, 127 (1994).